

Article

Black Phosphorus/WS₂-TM (TM: Ni, Co) Heterojunctions for Photocatalytic Hydrogen Evolution under Visible Light Illumination

Eminegül Genc Acar ^{1,†}, Seda Yılmaz ^{2,3,†}, Zafer Eroglu ² , İlknur Aksoy Çekceoğlu ¹, Emre Aslan ⁴ ,
İmren Hatay Patır ^{1,*} and Onder Metin ^{2,3,5,*}

¹ Department of Biotechnology, Selçuk University, 42250 Konya, Turkey; glgnc13@gmail.com (E.G.A.); ilknuraksoy1@gmail.com (İ.A.Ç.)

² Department of Chemistry, College of Sciences, Koç University, 34450 Istanbul, Turkey; sedayilmaz19@ku.edu.tr (S.Y.); zeroглу@ku.edu.tr (Z.E.)

³ Koç University Tüpraş Energy Center (KUTEM), Koç University, 34450 Istanbul, Turkey

⁴ Department of Biochemistry, Selçuk University, 42250 Konya, Turkey; emreaslan89@gmail.com

⁵ Koç University Surface Science and Technology Center (KUYTAM), Koç University, 34450 Istanbul, Turkey

* Correspondence: imrenhatay@gmail.com (İ.H.P.); ometin@ku.edu.tr (O.M.)

† These authors contributed equally to the work.

Abstract: Black phosphorus (BP) has recently emerged as a versatile photocatalyst owing to its unique photophysical properties and tunable bandgap. Nonetheless, the rapid recombination of the photogenerated charges of pristine BP samples has significantly hindered its practical applications in photocatalysis. Herein, we report, for the first time, the effect of transition metal nanoparticles (Ni and Co) as co-catalysts on the photocatalytic activity of BP/tungsten disulfide (WS₂) binary heterojunctions (BP/WS₂-TM (TM: Ni, Co)) in the hydrogen evolution reaction (HER) under visible light irradiation ($\lambda > 420$ nm). Ternary heterojunctions named BP/WS₂-TM (TM: Ni, Co) were synthesized via a chemical reduction method, leading to the formation of an S-scheme heterojunction, in which BP acts as a reduction catalyst and WS₂ serves as an oxidation catalyst. BP/WS₂-Ni and BP/WS₂-Co performed substantial amounts of hydrogen generation of 9.53 mmol h⁻¹g⁻¹ and 12.13 mmol h⁻¹g⁻¹, respectively. Moreover, BP/WS₂-Co exhibited about 5 and 15 times higher photocatalytic activity compared to the binary BP/WS₂ heterojunctions and pristine BP, respectively. The enhanced photocatalytic activity of the heterojunction catalysts is attributed to the extended light absorption ability, enhanced charge separation, and larger active sites. This study is the first example of photocatalytic hydrogen evolution from water by using Ni- and Co-doped binary BP/WS₂ heterojunctions.

Keywords: black phosphorus; tungsten disulfide; heterojunction photocatalyst; hydrogen evolution reaction; photocatalysis; solar hydrogen



Citation: Acar, E.G.; Yılmaz, S.; Eroglu, Z.; Çekceoğlu, İ.A.; Aslan, E.; Patır, İ.H.; Metin, O. Black Phosphorus/WS₂-TM (TM: Ni, Co) Heterojunctions for Photocatalytic Hydrogen Evolution under Visible Light Illumination. *Catalysts* **2023**, *13*, 1006. <https://doi.org/10.3390/catal13061006>

Academic Editors: Anna Kubacka and Zhenfeng Bian

Received: 10 April 2023

Revised: 6 June 2023

Accepted: 12 June 2023

Published: 14 June 2023



Copyright: © 2023 by the authors. Licensee MDPI, Basel, Switzerland. This article is an open access article distributed under the terms and conditions of the Creative Commons Attribution (CC BY) license (<https://creativecommons.org/licenses/by/4.0/>).

1. Introduction

Carbon-free hydrogen, namely green hydrogen, has been considered as a representative of the next-generation clean energy carriers owing to its remarkable properties including superior energy density per unit mass/volume, and environmental friendliness. Following the revolutionary study by Fujishima and Honda [1], solar-light-driven photocatalytic water splitting has attracted attention as a promising strategy for high-yield hydrogen production [2–7]. Current progress in this technology involves the development of earth-abundant, low-priced, non-toxic, and stable photocatalysts for both the hydrogen evolution reaction (HER) and the oxygen evolution reaction (OER). To date, numerous nanomaterials including metal sulfides [8], metal oxides [9–11], metal-free semiconductors (graphitic carbon nitride (g-CN), BP, etc.), and transition metal dichalcogenides (TMDs:

two-dimensional (2D) layered materials such as WS_2 , MoS_2 , and WSe_2) have been prepared to achieve efficient charge separation and transfer to provide high photocatalytic activity in water splitting [12–15]. Nevertheless, researchers are still making great efforts to develop ideal photocatalysts, such as those that have a high visible light absorption, lower electron–hole pair recombination rate, faster charge transport, and outstanding charge separation for more efficient photocatalytic HER [16]. Two-dimensional metal-free photocatalysts with enhanced visible light absorption have gained importance as new solar energy conversion materials because of their properties, such as cost efficiency, abundance, and a lack of toxicity [17–19]. In recent years, BP has obtained strong attention in photocatalysis as a metal-free semiconductor due to its unique physicochemical properties, which include strong anisotropic light–matter interaction, excellent light absorption (from ultraviolet (UV) to infrared (IR)), and a unique orthorhombic crystal shape [18,20]. However, some fundamental limitations of the pristine BP such as weak hydrogen adsorption capacity, a fast recombination rate of charge carriers, lack of surface active sites, narrow band gap, and easy degradation lead to insufficient photocatalytic hydrogen generation [21]. Various techniques such as doping with metal or non-metal ions [22,23], adding suitable nanostructures of co-catalysts [24,25], metal loading [26,27], and construction heterojunctions with other semiconductors [28] have been developed to overcome the shortcomings of BP. On the other hand, 2D-layered transition metal disulfides (TMDs), which consist of S–M–S layers connected by intramolecular bonds, have been considered fascinating candidates for photocatalysis due to their unique optical and electrical properties [29–36]. WS_2 , which is a member of the layered 2D metal dichalcogenides, has promising catalytic activity for HER due to its intrinsic properties such as tunable morphology, broad spectral range from NIR to UV, and strong W–S bonding [30,32]. WS_2 and BP could form a binary heterojunction with higher light absorption, charge separation, and reactive centers, which offer remarkable efficiency and stability in photocatalytic water splitting [37].

Photocatalytic HER in the presence of a noble-metal-free BP/ MoS_2 nanohybrid was investigated using CdS nanorods as light sensitizers under solar light irradiation. CdS/BP- MoS_2 nanohybrids showed remarkable photocatalytic activity with a $183.24 \text{ mmol h}^{-1} \text{ g}^{-1}$ hydrogen amount, and catalytic stability, which were attributed to the abundant active sites, high light absorption ability, and improved charge carrier mobility [38]. Moreover, BP/ MoS_2 photocatalysts were prepared using BP samples for solar HER. A substantial hydrogen evolution rate of $341 \text{ } \mu\text{mol h}^{-1} \text{ g}^{-1}$ was obtained by irradiating the BP/ MoS_2 with $>550 \text{ nm}$ light. In addition, the optimized BP/ MoS_2 generated $1286 \text{ } \mu\text{mol h}^{-1} \text{ g}^{-1}$ hydrogen when illuminated with visible light ($\lambda > 420 \text{ nm}$). This study showed that the photocatalytic performance of BP is affected positively with a reduced number of layers, since the less layered BP nanosheets have a much wider bandgap [18]. Furthermore, the 2D BP/ WS_2 heterojunction was reported as a noble-metal-free NIR-driven photocatalyst for the photocatalytic HER. BP/ WS_2 produced 2.49 and $1.55 \text{ } \mu\text{mol}$ hydrogen under $>780 \text{ nm}$ and 808 nm NIR laser irradiation, respectively, which was higher than that of pristine BP and WS_2 [30]. However, it has been shown that earth-abundant transition metal nanoparticles (NPs) can affect the photocatalytic activity of semiconductor photocatalysts by providing more active sites, light absorption, and charge separation [39]. Considering the effect of transition metal NPs as co-catalysts on BP/TMDs heterojunctions, to the best of the authors' knowledge, there is no report on the investigation of transition metal modification on the BP/ WS_2 heterojunctions to improve their photocatalytic HER activity.

In this context, we report, for the first time, the preparation of ternary heterojunctions doped with first-row transition metals (BP/ WS_2 -TM (TM: Ni, Co)) for photocatalytic HER under visible light irradiation. The photocatalytic activities of the heterojunction catalysts were investigated by using eosin-Y (EY) and triethanolamine (TEOA) as a sensitizer and sacrificial agent, respectively, under visible light irradiation ($\lambda > 420 \text{ nm}$). A highly stable and efficient noble-metal-free photocatalytic hydrogen production system was developed by using ternary heterojunctions compared to binary BP/ WS_2 heterojunctions. A significant increase in hydrogen production of about 4.2 and 5.4 times was obtained for BP/ WS_2 -Ni

and BP/WS₂-Co heterojunctions, respectively. The doping of the abundant Co co-catalyst on BP/WS₂ resulted in a solar-to-hydrogen (STH) efficiency of 31.2%, which can be explained by the enhanced light absorption capability, and thus improved enhanced charge transfer and separation efficiencies. This is the first application of BP/WS₂ heterostructures in photocatalytic HER, which can pave the way for 2D/2D heterojunction systems for energy applications.

2. Results and Discussion

2.1. Materials Characterization

To prepare BP/WS₂-TM (TM: Ni, Co) ternary heterojunction photocatalysts, a multistep method was used. This method involves (i) a synthesis procedure for BP/WS₂ heterojunctions, with the combination of WS₂ and pristine BP with different loading ratios (5, 10, 15, 20, 25, and 30 wt.%) nanosheets, created physically with the help of ultrasonic power, denoted as BP/WS₂-X (X presents BP contents); (ii) the impregnation of metal precursors into as-prepared BP/WS₂ heterojunctions in solution; and (iii) the chemical reduction of the impregnated metal ions in BP/WS₂ heterojunctions to generate Ni or Co nanoparticles (NPs). After the best photocatalytic activity was obtained with BP/WS₂-25 based on the hydrogen evolution reaction, the advanced characterization of this binary heterojunction was carried out as follows. TEM and EDS elemental mapping analysis were used to analyze the morphology and elemental distribution of all synthesized materials (Figure 1). The TEM images of pristine BP and WS₂ are shown in Figure 1a,b, respectively. From the TEM images, it can be seen that BP has a 2D layered structure (Figure 1a) with an average lateral size of 400 nm, while the pristine WS₂ consists of a nanorod-like shape with an average length of 15–20 nm (Figure 1b). There is no noticeable morphology change observed on the BP and WS₂ after their combination to yield BP/WS₂ binary heterojunctions, indicating that pristine BP nanosheets and WS₂ nanorods are uniformly assembled through the preservation of their initial morphologies (Figure 1c). The TEM images of metal-decorated nanocomposites are shown in Figure 1d,e (BP/WS₂-Ni) and Figure 1f (BP/WS₂-Co). The BP nanosheets and the formed NPs are clearly visible in the related TEM images, particularly in Figure 1e,f, where the formed Ni and Co NPs have an average particle size of 3 ± 0.5 nm. In addition to the TEM images, the HAADF-STEM images associated with the EDS elemental mapping images of BP/WS₂-Ni (5 wt%) and BP/WS₂-Co (0.5 wt%) heterojunctions (Figure 1g,h and Figure S1a,b (in the Supplementary Materials)) revealed that the ternary composites contain P, W, S, Ni, or Co elements in their structures, respectively. The EDS mapping images attributed to the P element of BP spread homogeneously, while the W and S elements originating from WS₂ are distributed in closed regions. According to Figure 1g,h, Ni and Co metals are mostly distributed homogeneously over the examined area. The elemental distributions of ternary BP/WS₂-TM (TM: Ni, Co) nanocomposites for an enlarged area were also studied using HAADF-STEM EDS mapping analysis, and the recorded images are depicted in Figure S1 (in the Supplementary Materials).

The crystal structure of the pristine materials and their heterojunctions was clarified via X-ray diffraction analysis. Figure 2 represents the recorded XRD patterns of BP, WS₂, BP/WS₂-25, BP/WS₂-Ni (5 wt%), and BP/WS₂-Co (0.5 wt%). The XRD pattern of pristine BP (Figure 2a) shows sharp peaks at $2\theta = 17.06^\circ, 26.76^\circ, 34.35^\circ, 34.54^\circ, 40.31^\circ,$ and 52.41° , which are readily assigned to the (020), (021), (040), (111), (041), and (060) crystal planes of the orthorhombic BP, respectively (JCPDS card no. 73-1358). There are no other peaks implying the presence of phosphorus oxides or other impurities [40]. As shown in Figure 2b, the as-prepared WS₂ depicts diffraction peaks at $2\theta = 13.89^\circ, 27.92^\circ, 34.16^\circ, 36.94^\circ, 40.31^\circ, 47.22^\circ, 49.52^\circ, 55.57^\circ,$ and 57.12° , which are attributed to the (002), (004), (100), (101), (003), (006), (105), (110), and (112) crystal planes of the well-known semiconducting 2H phase of WS₂ (2H-WS₂), respectively (JCPDS Card No: 08-0237) [41,42]. In addition to the 2H-WS₂ diffraction peaks, there is an obvious reflection peak observed at $2\theta = 13.89^\circ$ corresponding to the (002) reflection, thus pointing out that WS₂ nanostructures include multilayers [43]. After careful examination, two peaks were observed at $2\theta = 23.20^\circ$ and

23.78°, which are different from the characteristic peaks of the 2H-WS₂ phase. Zhou et al. reported that these two peaks were attributed to orthorhombic WO₃·H₂O (JCPDS Card No:43-0679), which is mostly formed during hydrothermal reaction conditions [44]. After the incorporation of BP into WS₂ to form BP/WS₂-25 binary heterojunctions, all the characteristic peaks of both BP and WS₂ were well preserved in the XRD pattern of BP/WS₂ heterojunctions (Figure 2c). Moreover, the peak at 2θ = 34.92°, assigned to the (111) plane of BP, appeared more intense, indicating a reduced number of BP layers after the exfoliation process and their incorporation into WS₂ [45]. Moreover, the XRD patterns of BP/WS₂-TM nanocomposites are shown in Figure 2d,e. No diffraction peaks corresponding to phases of Ni or Co, such as metals, metal oxides, or metal phosphides, were observed in the XRD patterns of either BP/WS₂-Co (0.5 wt%) or BP/WS₂-Ni (5 wt%), indicating the absence of these species. Moreover, the characteristic peak of WS₂ at 2θ = 13.89° attributed to the (002) plane disappeared after the incorporation of transition metal NPs with the chemical reduction method. It has been reported that the presence of (002) reflection indicates the interaction among the layers [46].

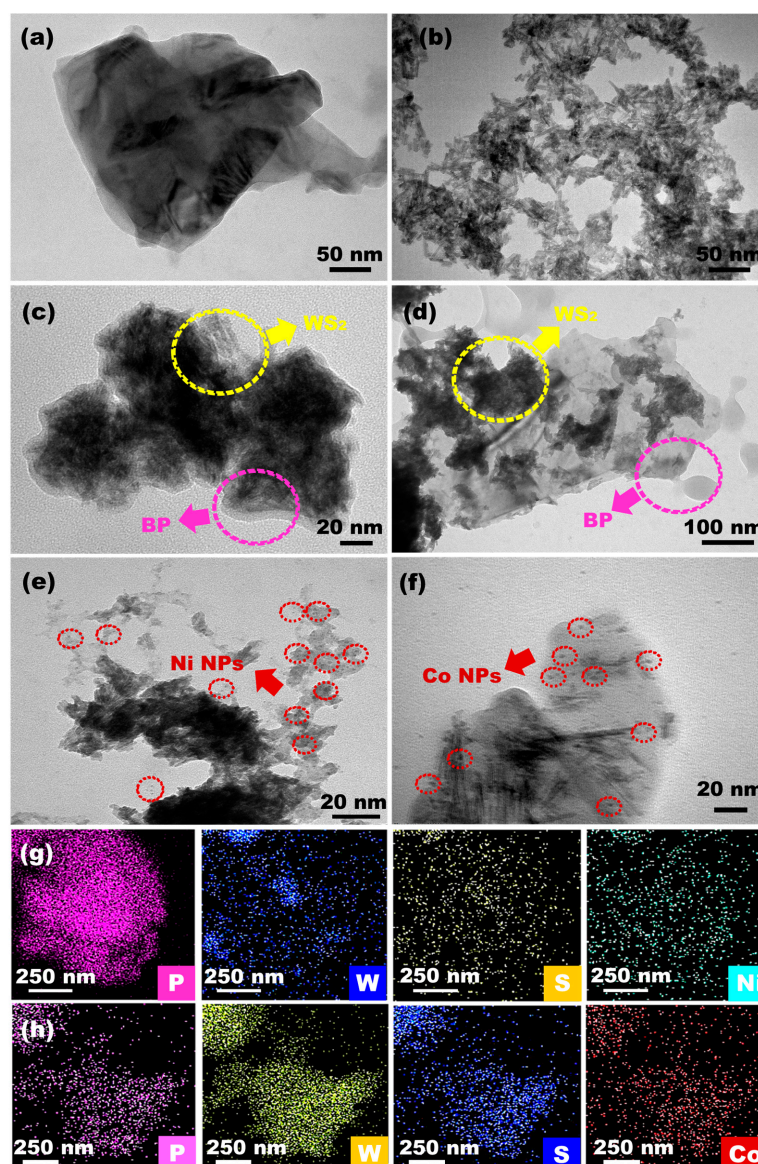


Figure 1. TEM images of (a) pristine BP, (b) pristine WS₂, (c) BP/WS₂-25, (d,e) BP/WS₂-Ni (5 wt%), (f) BP/WS₂-Co (0.5 wt%), and STEM-EDS elemental mapping images of BP/WS₂-Ni (5 wt%) (g) and BP/WS₂-Co (0.5 wt%) heterojunctions (h).

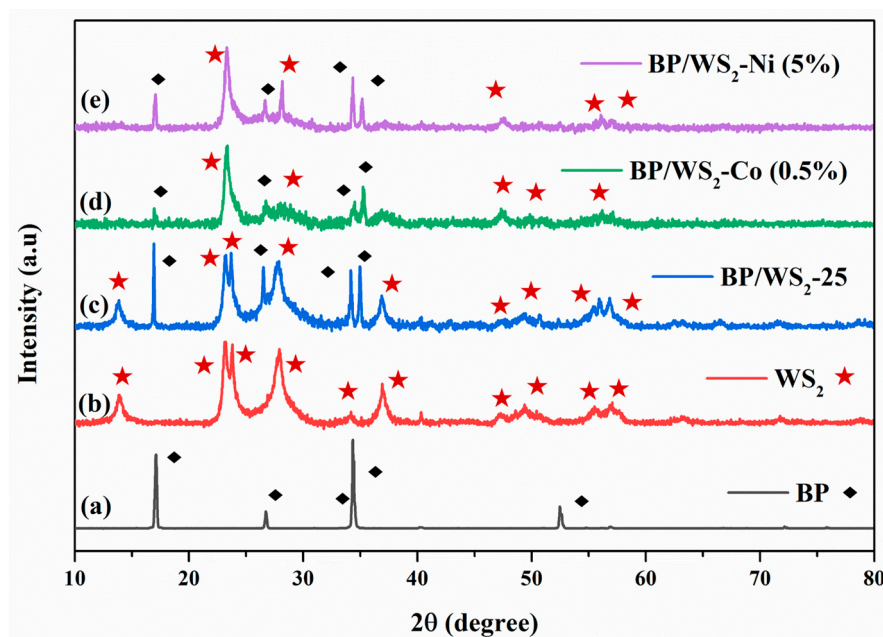


Figure 2. XRD patterns of (a) BP, (b) WS_2 , (c) BP/ WS_2 -25, (d) BP/ WS_2 -Co (0.5 wt%), and (e) BP/ WS_2 -Ni (5 wt%) nanocomposites (♦ indicates the BP planes while ★ indicates the planes of WS_2).

To understand the chemical composition and oxidation state of elements on the surface, X-ray photoelectron spectroscopy (XPS) was performed for BP/ WS_2 -25, BP/ WS_2 -Ni (5 wt%), and BP/ WS_2 -Co (0.5 wt%) nanocomposites. The XPS survey spectrum of the BP/ WS_2 -25, BP/ WS_2 -Ni (5 wt%), and BP/ WS_2 -Co (0.5 wt%) nanocomposites (Figures S1a and S2a,b (in the Supplementary Materials)) indicates that P 2p, W 4f, S 2p, and O 1s are located at their standard binding energies. The XPS spectrum of the P 2p region for BP/ WS_2 -Ni (5 wt%), shown in Figure 3a, is deconvoluted into four peaks. The peaks located at the binding energies of 129.2 and 130.1 eV correspond to P 2p_{3/2} and P 2p_{1/2} core levels, respectively. The peak at 133.9 eV is ascribed to oxidized phosphorus (P_xO_y) due to the reaction conditions used in the preparation process [30]. Moreover, the peak at 133.9 eV is indexed to the P-OH or P-H₂O which is present due to the reaction of BP and P_xO_y with water [45,47,48]. The core level of W 4f is shown in Figure 3b. The presence of 1T and/or 2H phases of WS_2 can be confirmed by XPS analysis [49]. In the W 4f region, the peaks located at 33.8 and 35.9 eV are assigned as W 4f_{7/2} and W 4f_{5/2} of the 1T phase WS_2 , respectively. In contrast, the relatively strong peaks located at 35.1 and 37.3 eV correspond to the W 4f_{7/2} and W 4f_{5/2} core levels of 2H- WS_2 , respectively [50]. Meanwhile, the peak at 40.7 eV is ascribed to the W 5p_{3/2} of W^{4+} in the WS_2 phase [51,52]. In the high-resolution XPS spectrum for the S 2p region, the two peaks observed at 162.6 and 163.9 eV are indexed to S 2p_{5/2} and S 2p_{3/2} for WS_2 , respectively (Figure 3c) [53]. Additionally, the two other higher binding energy peaks located at 169.0 and 170.3 eV are attributed to SO_x , which originates from the oxidation of sulfide ions during the synthesis process [44,51]. Figure 3d shows the core level spectrum of Ni 2p. In particular, the peaks at binding energies of 856.0 and 873.4 eV can be attached to the Ni^{2+} species, while the peaks at 858.5 and 875.4 eV are indexed to the Ni^{3+} species due to the excess oxygen from NiOOH [54], accompanied by its satellite peaks at 861.9 and 879.2 eV [55,56]. In addition, the small peaks at 852.9 and 860.7 eV could be assigned to metallic Ni^0 , indicating the presence of metallic Ni NPs. The presence of Ni NPs was also confirmed by TEM analysis [57,58]. The high-resolution XPS spectrum of BP/ WS_2 -Co (0.5 wt%) was also examined (Figure S3, in the Supplementary Materials). In the case of the Co 2p spectrum (Figure S4d in Figure S4 (in the Supplementary Materials)), the peaks at 782.0 and 797.0 eV belong to Co^{2+} 2p_{3/2} and Co^{2+} 2p_{1/2}, respectively, while the satellite peaks occur at 792.0 and 807.0 eV [59]. Additionally, the peaks at 787.0 and 802.1 eV demonstrate the appearance of cobalt hydroxide which can be attributed to the

oxidized Co species in the environment [60]. There is no peak that reveals the presence of metallic Co or Co nanoparticles (~ 779 eV) because of the low loading ratio of Co [61].

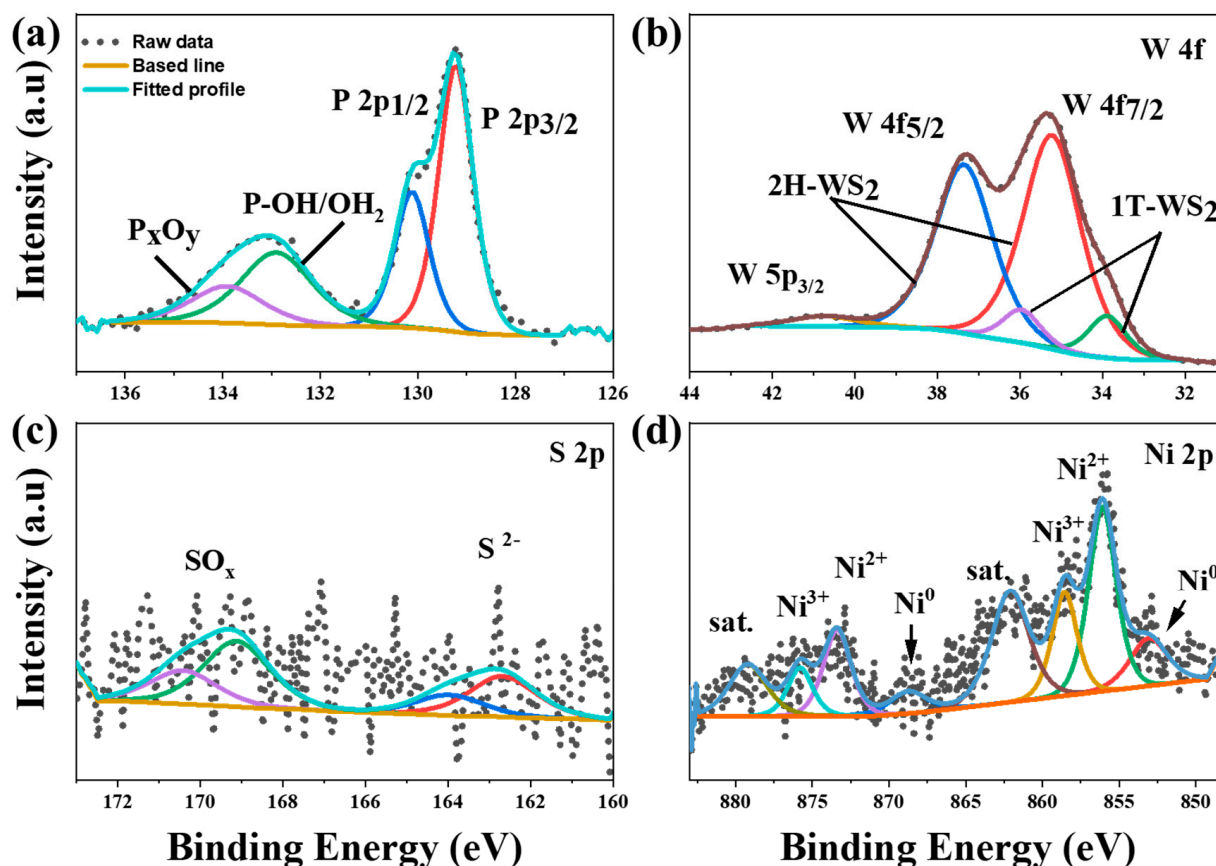


Figure 3. High-resolution XPS spectra of BP/WS₂-Ni (5 wt%) (a) P 2p, (b) W 4f, (c) S 2p, and (d) Ni 2p regions.

Steady-state photoluminescence (PL) analysis and lifetime analysis were accomplished to evaluate the efficiency of charge kinetics, and the recorded spectra are shown in Figure 4. Mainly, both lower steady-state PL intensity and longer lifetime of electron–hole pairs indicate higher photo-generated charge separation efficiency. As shown in Figure 4a, WS₂ has the highest emission curve, indicating the high recombination of photoexcited electron–hole pairs [62]. With the incorporation of BP and the transition metal, the emission intensity obviously decreased, as evidenced by the accelerated electron–hole separation. This result also matches well with the photocatalytic efficiency [63]. Lifetime measurements can be seen in Figure 4b. Pristine WS₂ has the highest lifetime (1.669 ns) compared to the BP/WS₂-25 (1.611 ns), BP/WS₂-Ni (5%) (0.711 ns), and BP/WS₂-Co (0.5%) (0.657 ns). These results indicate that the inclusion of Ni and Co NPs effectively diminishes the electron–hole lifetime which can be concluded from the enhanced charge transfer kinetics between nanoparticles and BP/WS₂ nanocomposites [64].

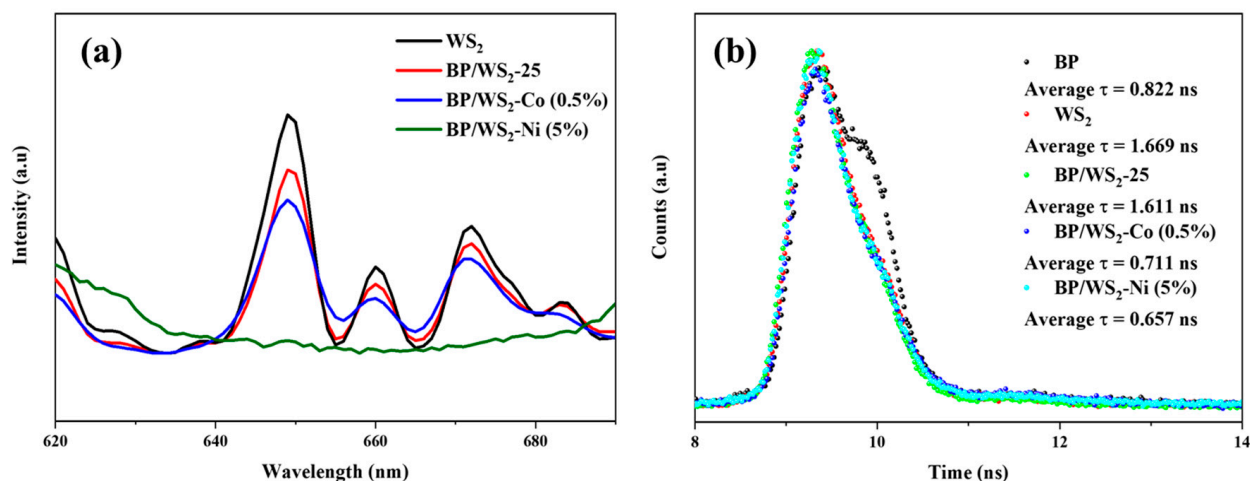


Figure 4. (a) Photoluminescence decay curves and (b) time resolved photoluminescence spectra of BP, WS₂, BP/WS₂-25, BP/WS₂-Ni (5 wt%), and BP/WS₂-Co (0.5 wt%) samples.

2.2. The Photocatalytic Hydrogen Evolution Studies

The photocatalytic hydrogen evolution activities of WS₂, BP, BP/WS₂, and ternary BP/WS₂-TM (Y: Ni and Co) nanocomposites were examined in the presence of TEOA (0.33 M, 5%) as a sacrificial agent and EY as a photosensitizer under visible light irradiation ($\lambda > 420$ nm). In the control experiments, it was found that no appreciable H₂ evolution was detected in the absence of reactants or light irradiation. The pristine BP and WS₂ samples showed low hydrogen production rates of 0.04 mmol h⁻¹g⁻¹ and 0.73 mmol h⁻¹g⁻¹, respectively, under visible light illumination, which can be ascribed to the intrinsic fast recombination of the photoinduced charge carriers. As shown in Figure S5 (in the Supplementary Materials), the effect of changing the ratio of BP loading on the photocatalytic hydrogen evolution activity of BP/WS₂ heterojunction was investigated by using a BP/WS₂ catalyst with six different BP mass ratios (BP/WS₂-5%, BP/WS₂-10%, BP/WS₂-15%, BP/WS₂-20%, BP/WS₂-25%, and BP/WS₂-30%) for 8 h. The loading with 25 wt% BP showed the best photocatalytic activity with 2.24 mmol h⁻¹g⁻¹, which is about three times higher compared to pristine BP. The excessive loading ratio of more than this negatively affected the HER activity of BP/WS₂. After 8 h of solar irradiation, the photocatalytic activity of optimized BP/WS₂ reached 13.32 mmol g⁻¹. The enhanced photocatalytic activity can be described by the large and intimate type-II heterojunction formed in BP/WS₂, which accelerates the photogenerated charge separation. WS₂ plays a role as an effective co-catalyst to enhance photocatalytic performance by trapping the photogenerated electrons from the excited BP [30]. The wavelength-dependent photocatalytic hydrogen production performance of BP/WS₂ binary heterojunctions was previously studied by Zhu and co-workers. According to their results, the HER of BP/WS₂ enhanced the photocatalytic HER activity under solar light ($\lambda > 420$ nm) compared to NIR light (from 600 to 1200 nm), which was attributed to weak light absorption and a light-dependent photoreaction at longer wavelengths. The photocatalytic activity of BP/WS₂ was 0.83 mmol h⁻¹g⁻¹, 0.51 mmol h⁻¹g⁻¹, and 3.2 mmol h⁻¹g⁻¹ under >780 nm, 808 nm, and solar light irradiation, respectively. Our results surpassed this pioneering study by developing highly stable ternary heterojunctions doped with first-row transition metals (BP/WS₂-TM (TM: Ni, Co)) for photocatalytic HER under visible light irradiation due to the improvement in the light absorption ability, charge carrier separation, and active sites [30].

To investigate the effect of transition metal nanoparticles on the photocatalytic activity of BP/WS₂ heterojunctions, the optimized BP/WS₂-25% was decorated with the earth abundant Ni and Co metals for highly-efficient HER. First, the photocatalytic studies of the ternary photocatalysts with five experimental Ni ratios (ranging from 1–8 wt%) based on the ICP-MS analysis were carried out under solar light. The 5 wt% Ni produced the highest

hydrogen production of $9.53 \text{ mmol h}^{-1}\text{g}^{-1}$ among all tested ratios (Figure 5a). After 8 h of the photocatalytic HER, the total hydrogen production for BP/WS₂-Ni reached $39.81 \text{ mmol h}^{-1}\text{g}^{-1}$. The inclusion of the Co co-catalyst into BP/WS₂ resulted in a hydrogen production of $12.13 \text{ mmol h}^{-1}\text{g}^{-1}$, and reached $43.91 \text{ mmol g}^{-1}$ after 8 h, which is the highest rate of comparable photocatalytic reactions with a 5.4 times greater amount of hydrogen than that of BP/WS₂ (Figure 5b). Figure 5c also compares the time-dependent photocatalytic hydrogen activities of the optimum rates for BP/WS₂, BP/WS₂-Ni and BP/WS₂-Co catalysts. BP/WS₂-TM (Y: Ni, Co) displayed improved photocatalytic H₂ evolution activity and stability compared to pristine BP and BP/WS₂. Consequently, Ni and Co were found to have a significant effect on the photocatalytic activity of BP/WS₂. The outstanding photocatalytic performance of BP/WS₂-Ni and BP/WS₂-Co ternary heterojunction photocatalysts is assigned to broader light absorption, effective charge separation, and increased active sites [65]. Moreover, the STH efficiencies of the catalysts were calculated using Equation (1), as shown in Section 3.3. The STH efficiencies were found to be 31.2%, 24.5%, 5.7%, 1.8%, and 0.1% for BP/WS₂-Co, BP/WS₂-Ni, BP/WS₂, BP, and WS₂, respectively, which is comparable to the photocatalytic hydrogen evolution activities. The photocatalytic HER rate of BP/WS₂-TM (TM: Ni, Co) was evaluated by comparing it with the relevant materials in the literature, as outlined in Table S1 (in the Supplementary Materials). It was observed that comparable results were obtained, consistent with those reported in the literature. Moreover, the stability of the optimized catalysts was investigated by repeating the photocatalytic tests over BP/WS₂-TM (Y: Ni and Co) three times under the same experimental conditions. After the third consecutive photocatalytic HER run, it was observed that the photocatalytic hydrogen activities of BP/WS₂-Ni and BP/WS₂-Co nanohybrids were maintained at 92.04% and 95.4%, respectively, as shown in Figure S6 (in the Supplementary Materials). The difference in the photostability of BP/WS₂, BP/WS₂-Ni or BP/WS₂-Co heterojunctions could be attributed to the degradation of EY. The UV-vis absorption analysis of BP/WS₂ heterojunctions sensitized with EY was compared after 8 h of excitation, as seen in Figure S7 (in the Supplementary Materials). The characteristic peak of EY shifted from 520 nm to about 490 nm, with decreasing peak intensity after the photocatalytic hydrogen production reaction. The decrease in peak intensity indicates dye degradation [66], which is due to the elimination of bromines from EY structures, resulting in fluorescein-based structures [67,68]. The UV-vis absorption results are consistent with the photocatalytic hydrogen evolution activities of the catalysts, as well as their stabilities. Similarly, the absorption spectral results of BP/WS₂-Ni and BP/WS₂-Co catalysts were found to be compatible with the photocatalytic hydrogen production amounts determined for these catalysts (Figures S8 and S9 (in the Supplementary Materials)).

Based on the above results, a possible charge migration mechanism for the solar-driven photocatalytic HER of ternary catalysts (BP/WS₂-TM; Y: Ni, Co) was proposed considering the band gap and the position of the electronic energy levels of the catalysts [69], as shown in Figure 6. A step-scheme (S-scheme) was proposed for the charge transfer at the interface between BP and WS₂ under visible light irradiation, which resulted in an effective charge separation and promoted the improvement in photocatalytic performance. The pristine BP shows a low photocatalytic hydrogen production activity due to the intrinsic fast recombination of photogenerated charge carriers. Upon the absorption of visible light, the excitation of EY occurs in three main sequential steps. First, EY is excited to the singlet state EY1*. Then, inter system crossing (ISC) leads to a more stable triplet state of 3EY*. Finally, the reaction of EY3* with the TEOA sacrificial agent result in EY^{-•}. After the loss of the electron, the conversion of EY^{-•} to the ground state EY occurs [70,71]. Subsequently, the excited electrons in the EY intermediate forms are transferred to the conduction band (CB) of BP because they have a higher potential than that of BP or WS₂. According to the S-scheme heterojunction, the electron transfers have resulted in an S-scheme based on the energy band levels calculated in our previous studies [72,73]. Here, the photogenerated electrons on the CB of WS₂ are directly transferred to VB of BP because the position of CB of WS₂ is slightly higher than that of VB of BP. They are close enough for direct electron

transfer, resulting in the effective separation of the photogenerated charge carriers [17]. The synergism formed at the heterointerface of BP and Ni/CoS_x in the BP/WS₂-xNiS_x ternary heterojunction could facilitate the transfer of the photogenerated electrons via the sulfur bridges, resulting in a decreased recombination of e⁻ and h⁺ [72,73]. In this regard, BP plays a role as an electron sink that enhances the photocatalytic activity by decreasing the recombination of the photogenerated electron-hole pair due to the S-scheme electron transfer mechanism [74]. Hydrogen evolution can easily take place due to the CB levels of BP, which are more negative than the reduction potential of H⁺/H₂ (0 V vs. NHE) [75]. At the same time, the TEOA sacrificial agent provides electrons for holes on the VB of WS₂ for the regeneration of the photocatalytic reaction, effectively inhibiting the recombination process of electron-hole pairs. WS₂ plays the role of an electron pathway through the S-W-S atomic planes, which enhances the electron transfer between the semiconductor photocatalysts [76].

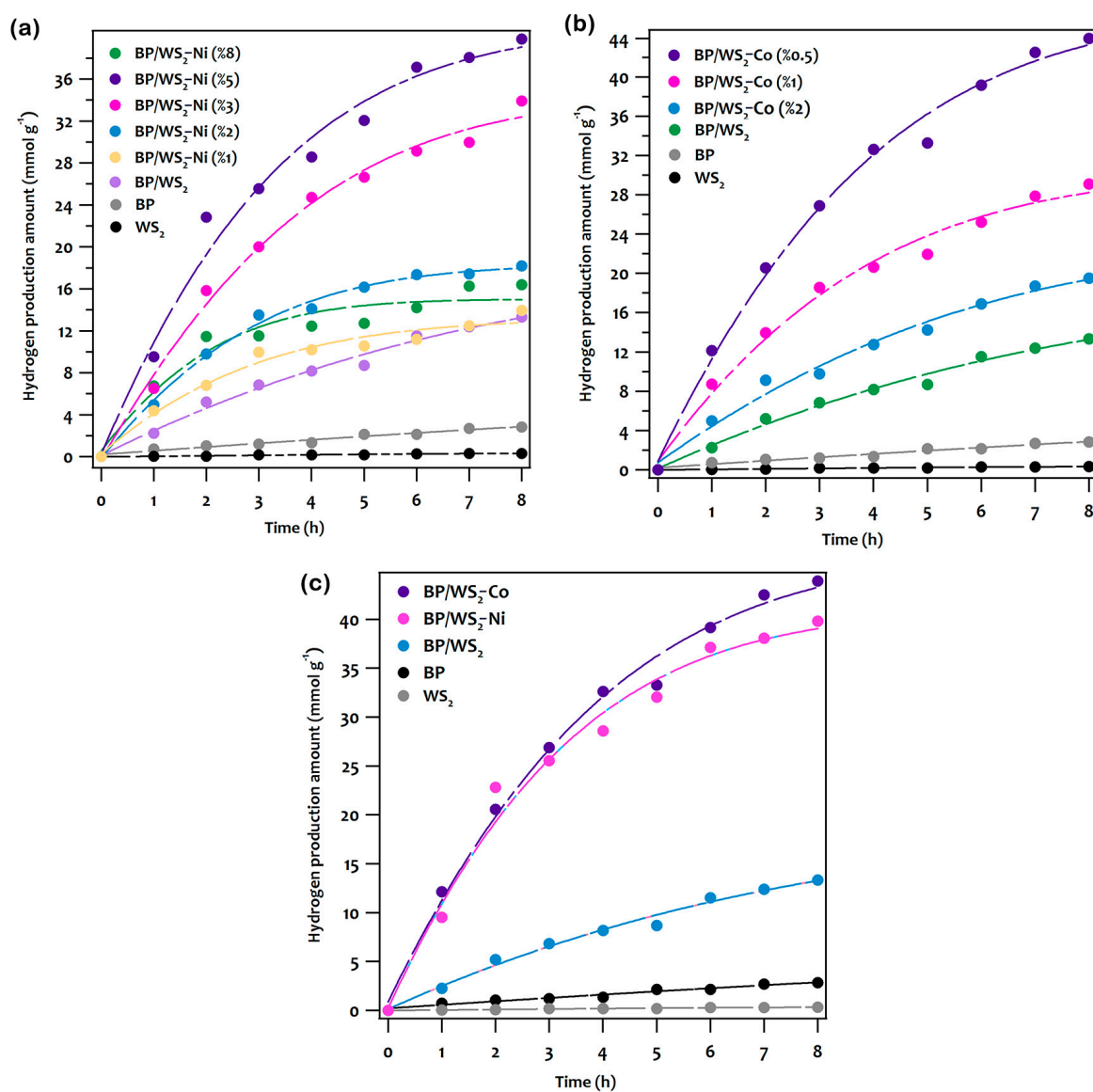


Figure 5. Comparison of photocatalytic hydrogen evolution activities of BP/WS₂ nanocomposites at various Ni (a) and Co (b) amounts with the BP and BP/WS₂ nanocomposite form (c) in the presence of TEOA (0.33 M, 5%) sacrificial agent by using EY (3.25×10^{-4} M) under visible light irradiation ($\lambda > 420$ nm).

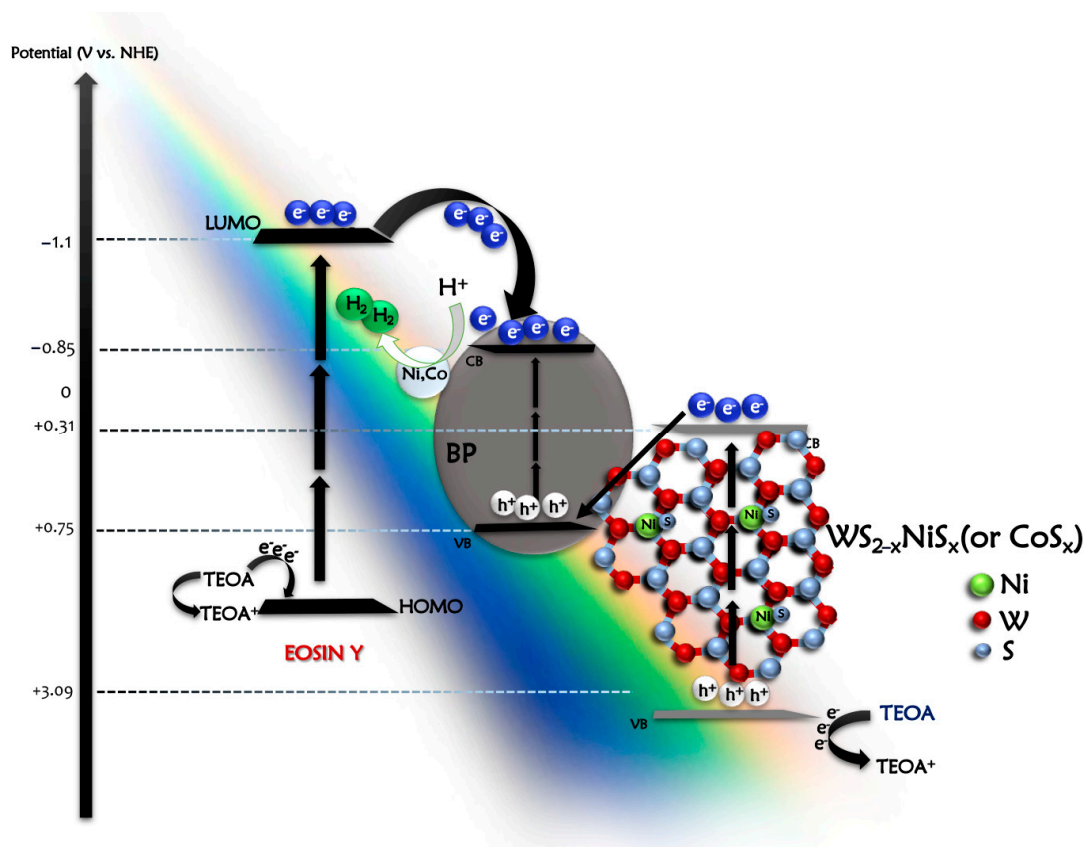


Figure 6. The mechanisms of solar-driven photocatalytic HER proposed for BP/WS₂-TM; (Y: Ni or Co) nanocomposites in the presence of EY and TEOA as the sensitizer and sacrificial agent, respectively.

3. Experimental Section

3.1. Materials and Chemicals

Tungsten (VI) chloride (WCl₆, ≥99.9%) was purchased from Sigma-Aldrich, Darmstadt, Germany. Red phosphorus (98.9%), nickel (II) acetate tetrahydrate (Ni(CH₃COO)₂·4H₂O, 98+%), cobalt (II) acetate tetrahydrate (Co(OOCCH₃)₂·4H₂O, 98%), and copper acetate (Cu(ac)₂) were purchased from Alfa Aesar, Kandel, Germany. N, N-dimethylformamide (DMF) and ethanol (absolute) were purchased from Merck, Darmstadt, Germany. Thioacetamide (C₂H₅NS, 99%) was purchased from J&K-Scientific, San Jose, CA, USA. All chemicals were used as received.

3.2. The Material Synthesis

3.2.1. The Synthesis of Crystalline BP and Few-Layer BP

Black phosphorous crystals were synthesized by utilizing the well-established low-pressure chemical transport method, which is described in one of our publications [73]. The details of synthesis can be found in the Supplementary Materials as well.

3.2.2. The Synthesis of WS₂

Pristine WS₂ were prepared by using a simple hydrothermal method [77]. In a typical synthesis recipe, after dissolving a determined quantity of tungsten (VI) chloride and sodium thioacetamide (WCl₆:C₂H₅NS = 1:2) in 30 mL of distilled water, the resulting homogeneous solution was transferred to a Teflon-lined stainless-steel autoclave for hydrothermal treatment. The autoclave was then placed into a furnace and heated at 180 °C for 16 h. After cooling down to room temperature, the obtained mixture was separated by using centrifugation at 9000 rpm for 10 min and cleansed with ethanol and dried in vacuo.

3.2.3. The Fabrication of BP/WS₂ Binary Nanocomposites

BP/WS₂ binary nanocomposites were prepared via a simple liquid-phase self-assembly method [45]. In the typical synthesis procedure, as-prepared pristine WS₂ powder (20 mg) was dispersed in a DMF solution (40 mL) using an ultrasonic bath. A specific amount of BP/DMF stock solution prepared in advance was added dropwise into the WS₂/DMF dispersion and kept under ultrasonication for about 3–4 h. The yielded mixture was centrifuged, separated from its residuals, and dried under vacuum.

3.2.4. The Fabrication of BP/WS₂-TM (TM: Ni, Co) Ternary Nanocomposites

The synthesis of transition metal-doped BP/WS₂ nanocomposites (BP/WS₂-TM) was performed using a two-step procedure comprising the liquid-phase impregnation of metal precursors into the BP/WS₂ followed by a chemical reduction of metal ions by NaBH₄. The information related to the preparation method was described for the synthesis of m-gCN/BP-TM heterojunctions in one of our publications [73] and the details can be acquired in the SI. The optimized and characterized ternary nanocomposites were determined as BP/WS₂-Ni (5 wt%), and BP/WS₂-Co (0.5 wt%), where (X wt%) defines the theoretical values of the loaded transition metals on the binary nanocomposites.

3.3. The Photocatalytic Hydrogen Evolution Reaction (HER)

The photocatalytic hydrogen evolution performances of the prepared materials were investigated in the presence of EY using TEOA as a sacrificial agent under visible light irradiation for 8 h. TEOA (0.33 M, 5%) and EY solutions (3.25×10^{-4} M) were prepared in aqueous medium and placed in the glove box. The deoxygenated TEOA (20 mL) and EY (1.3 mL) were added to the catalysts in the quartz reaction flask (about 135 mL volume). The mixture was then returned to room conditions by sealing it with a rubber septum and it was homogenized under ultrasonic treatment. The photocatalytic activities were studied by placing the reactor in front of the Solar Light-XPS 300TM, Philadelphia, PA, United States, (with cut-off filter $\lambda \geq 420$ nm) under continuous stirring. The produced hydrogen gas was detected using Shimadzu GC-2010 Plus gas chromatography with a thermal conductivity detector (TCD) and using argon as a carrier gas, which was realized hourly with a syringe from the headspace of the flask. The photocatalytic-HER performance of the catalysts was demonstrated by calculating the STH efficiencies as shown in Equation (1). The equation is defined as

$$\text{STH (\%)} = \left[\frac{R_{H_2} \Delta G^\circ}{P A} \right] 100 \quad (1)$$

where R_{H_2} is the amount of hydrogen (mmol hydrogen/s), ΔG° is the Gibbs free energy for the production of one mole of hydrogen (J/mol), P is the intensity of the sunlight (mW/cm^2), and A is the irradiation area (cm^2), respectively [78].

4. Conclusions

In summary, we have successfully prepared 2D/2D BP/WS₂ binary heterojunctions and intensively investigated their photocatalytic activity in HER for the first time with and without transition-metal incorporation under visible light irradiation (≥ 420 nm). It is well known that the intrinsic fast recombination of photoinduced charge carriers of the pristine BP resulted in a weak photocatalytic activity in the HER. The characterization of the optimal binary and ternary forms of BP/WS₂-based heterojunctions revealed that an S-scheme heterojunction was formed between BP and WS₂. Here, compared to pristine BP, an approximately three times higher hydrogen quantity was obtained with the BP/WS₂ heterojunction catalyst, with a STH efficiency of 5.7%, which was attributed to the large contact areas providing many channels for photogenerated charge transfer. In addition, the incorporation of earth-abundant transition metal (Ni or Co) NPs further enhanced the photocatalytic HER activity of BP/WS₂ binary nanocomposites. The loading of an earth-abundant Co as a co-catalyst in BP/WS₂ binary heterojunction resulted in an STH efficiency of 31.2%, which can be attributed to the achievement of more photon absorption,

more active sites, and a longer charge carrier lifetime through decreasing the recombination rate. Considering the 8h photocatalytic activities of BP/WS₂-TM (TM: Ni or Co) ternary heterojunction catalysts, we observed 3.2 times and 2.9 times more hydrogen with BP/WS₂-Ni and BP/WS₂-Co, respectively, compared to BP/WS₂. This noble-metal-free catalyst system demonstrated highly stable and efficient photocatalytic hydrogen production through the deposition of transition metal NPs (especially Co NPs) on the BP/WS₂ heterojunction. The current study points out that BP/WS₂ binary heterojunctions possess more specific active sites and hence higher photocatalytic efficiency than pristine BP nanosheets in HER under visible light irradiation. Moreover, this study clearly demonstrated that the photocatalytic hydrogen evolution activity of the BP/WS₂ heterojunction can be further improved through the loading of non-precious transition metals. We anticipate that this study will open ways for the development of highly efficient, cost effective, and solar-driven hydrogen production techniques and other potential energy applications.

Supplementary Materials: The following supporting information can be downloaded at: <https://www.mdpi.com/article/10.3390/catal13061006/s1> Instrumentation, The Materials Preparation; Figure S1. STEM images of (a) BP/WS₂-Ni (5%) and (b) BP/WS₂-Co (0.5%); Figure S2. High resolution XPS spectra of BP/WS₂-25 binary nanocomposites: (a) survey, (b) P 2p, (c) W 4f, and (d) S 2p; Figure S3. Survey spectra of (a) BP/WS₂-Ni (5%), and (b) BP/WS₂-Co (0.5%) nanocomposites; Figure S4. High resolution XPS spectra of BP/WS₂-Co (0.5%) nanocomposites: (a) P 2p, (b) W 4f, (c) S 2p, and (d) Co 2p; Figure S5. The BP loading effect on BP/WS₂ heterojunction by using different BP mass ratios in the presence of TEOA (0.33 M, 5%) and EY (3.25×10^{-4} M) as a sacrificial agent and sensitizer, respectively, under visible illumination (≥ 420 nm) for 8 h; Figure S6. Stability study of hydrogen evolution over BP/WS₂-Ni and BP/WS₂-Co heterojunctions under visible light irradiation; Figure S7. UV-vis spectra of BP, WS₂, and BP/WS₂ nanocomposites with different BP mass ratios in the presence of EY before and after photocatalytic reactions; Figure S8. UV-vis spectra of BP, WS₂, and BP/WS₂ nanocomposites with different Ni mass ratios (from 1% to 8%) in the presence of EY before and after photocatalytic reactions; Figure S9. UV-vis spectra of BP, WS₂, and BP/WS₂ nanocomposites with different Co mass ratios (0.5%, 1%, and 2%) in the presence of EY before and after photocatalytic reactions; Table S1. The comparison of BP/WS₂-TM; (TM: Ni, Co) heterojunction photocatalysts with similar materials that were tested in the photocatalytic HER in the literature. References [18,24,38,39,79–85] are cited in the Supplementary Materials.

Author Contributions: Methodology, E.G.A. and S.Y.; formal analysis, E.G.A., S.Y., Z.E. and İ.A.Ç.; investigation, E.G.A., S.Y., Z.E., İ.A.Ç. and E.A.; visualization, E.G.A., S.Y., Z.E., İ.A.Ç. and E.A.; writing—original draft, E.G.A., S.Y., Z.E., İ.A.Ç., E.A., İ.H.P. and O.M.; validation, Z.E. and E.A.; conceptualization, E.A., İ.H.P. and O.M.; supervision, E.A., İ.H.P. and O.M.; writing—review and editing, İ.H.P. and O.M.; project administration, E.A., İ.H.P. and O.M.; funding acquisition, E.A., İ.H.P. and O.M. All authors have read and agreed to the published version of the manuscript.

Funding: This research was funded by The Scientific and Technological Research Council of Turkey (TUBITAK, Project No: 119Z497).

Data Availability Statement: Data are available upon reasonable request.

Acknowledgments: The authors would like to thank Selcuk University Scientific Research Projects office (20211014) for partially supporting this work. This paper is part of a PhD thesis prepared by Eminegül Genc Acar.

Conflicts of Interest: The authors declare no conflict of interest.

References

1. Fujishima, A.; Honda, K. Electrochemical photolysis of water at a semiconductor electrode. *Nature* **1972**, *238*, 37–38. [[CrossRef](#)]
2. Jafari, T.; Moharreri, E.; Amin, A.S.; Miao, R.; Song, W.; Suib, S.L. Photocatalytic water splitting—The untamed dream: A review of recent advances. *Molecules* **2016**, *21*, 900. [[CrossRef](#)] [[PubMed](#)]
3. Darkwah, W.K.; Oswald, K.A. Photocatalytic applications of heterostructure graphitic carbon nitride: Pollutant degradation, hydrogen gas production (water splitting), and CO₂ reduction. *Nanoscale Res. Lett.* **2019**, *14*, 234. [[CrossRef](#)] [[PubMed](#)]
4. Ismail, A.A.; Bahnemann, D.W. Photochemical splitting of water for hydrogen production by photocatalysis: A review. *Sol. Energy Mater. Sol. Cells* **2014**, *128*, 85–101. [[CrossRef](#)]

5. Ran, J.; Zhang, J.; Yu, J.; Jaroniec, M.; Qiao, S.Z. Earth-abundant cocatalysts for semiconductor-based photocatalytic water splitting. *Chem. Soc. Rev.* **2014**, *43*, 7787–7812. [[CrossRef](#)] [[PubMed](#)]
6. Zou, X.; Zhang, Y. Noble metal-free hydrogen evolution catalysts for water splitting. *Chem. Soc. Rev.* **2015**, *44*, 5148–5180. [[CrossRef](#)]
7. Zhang, G.; Lan, Z.A.; Wang, X. Conjugated polymers: Catalysts for photocatalytic hydrogen evolution. *Angew. Chem. Int. Ed.* **2016**, *55*, 15712–15727. [[CrossRef](#)]
8. Zhang, K.; Kim, J.K.; Ma, M.; Yim, S.Y.; Lee, C.L.; Shin, H.; Park, J.H. Delocalized electron accumulation at nanorod tips: Origin of efficient H₂ generation. *Adv. Funct. Mater.* **2016**, *26*, 4527–4534. [[CrossRef](#)]
9. Wang, X.; Xu, Q.; Li, M.; Shen, S.; Wang, X.; Wang, Y.; Feng, Z.; Shi, J.; Han, H.; Li, C. Photocatalytic overall water splitting promoted by an α - β phase junction on Ga₂O₃. *Angew. Chem.* **2012**, *124*, 13266–13269. [[CrossRef](#)]
10. Lin, Z.; Xiao, J.; Li, L.; Liu, P.; Wang, C.; Yang, G. Nanodiamond-embedded p-type copper (I) oxide nanocrystals for broad-spectrum photocatalytic hydrogen evolution. *Adv. Energy Mater.* **2016**, *6*, 1501865. [[CrossRef](#)]
11. Núñez, J.; Fresno, F.; Platero-Prats, A.E.; Jana, P.; Fierro, J.L.; Coronado, J.M.; Serrano, D.P.; de la Peña O’Shea, V.A. Ga-promoted photocatalytic H₂ production over Pt/ZnO nanostructures. *ACS Appl. Mater. Interfaces* **2016**, *8*, 23729–23738. [[CrossRef](#)]
12. Zong, X.; Han, J.; Ma, G.; Yan, H.; Wu, G.; Li, C. Photocatalytic H₂ evolution on CdS loaded with WS₂ as cocatalyst under visible light irradiation. *J. Phys. Chem. C* **2011**, *115*, 12202–12208. [[CrossRef](#)]
13. Jia, Z.; Lyu, F.; Zhang, L.; Zeng, S.; Liang, S.; Li, Y.; Lu, J. Pt nanoparticles decorated heterostructured g-C₃N₄/Bi₂MoO₆ microplates with highly enhanced photocatalytic activities under visible light. *Sci. Rep.* **2019**, *9*, 7636. [[CrossRef](#)] [[PubMed](#)]
14. Zheng, Y.; Chen, Y.; Gao, B.; Lin, B.; Wang, X. Black phosphorus and carbon nitride hybrid photocatalysts for photoredox reactions. *Adv. Funct. Mater.* **2020**, *30*, 2002021. [[CrossRef](#)]
15. Strmcnik, D.; Lopes, P.P.; Genorio, B.; Stamenkovic, V.R.; Markovic, N.M. Design principles for hydrogen evolution reaction catalyst materials. *Nano Energy* **2016**, *29*, 29–36. [[CrossRef](#)]
16. Bashir, S.; Iqbal, N.; Jamil, A.; Alazmi, A.; Shahid, M. Facile synthesis of a novel photocatalyst with integrated features for industrial effluents treatment. *Ceram. Int.* **2022**, *48*, 3172–3184. [[CrossRef](#)]
17. Liu, F.; Huang, C.; Liu, C.X.; Shi, R.; Chen, Y. Black Phosphorus-Based Semiconductor Heterojunctions for Photocatalytic Water Splitting. *Chem. Eur. J.* **2020**, *26*, 4449–4460. [[CrossRef](#)] [[PubMed](#)]
18. Yuan, Y.-J.; Wang, P.; Li, Z.; Wu, Y.; Bai, W.; Su, Y.; Guan, J.; Wu, S.; Zhong, J.; Yu, Z.-T. The role of bandgap and interface in enhancing photocatalytic H₂ generation activity of 2D-2D black phosphorus/MoS₂ photocatalyst. *Appl. Catal. B Environ.* **2019**, *242*, 1–8. [[CrossRef](#)]
19. Ozer, M.S.; Eroglu, Z.; Yalin, A.S.; Kılıç, M.; Rothlisberger, U.; Metin, O. Bismuthene as a versatile photocatalyst operating under variable conditions for the photoredox CH bond functionalization. *Appl. Catal. B Environ.* **2022**, *304*, 120957. [[CrossRef](#)]
20. Altan, O.; Eroğlu, Z.; Küçükkeçeci, H.; Metin, Ö. Black phosphorus-based photocatalysts for energy and environmental applications. In *Nanostructured Photocatalysts*; Elsevier: Amsterdam, The Netherlands, 2021; pp. 421–449.
21. Xue, Y.; Min, S.; Wang, F. Dye-sensitized black phosphorus nanosheets decorated with Pt cocatalyst for highly efficient photocatalytic hydrogen evolution under visible light. *Int. J. Hydrogen Energy* **2019**, *44*, 21873–21881. [[CrossRef](#)]
22. Lv, W.; Yang, B.; Wang, B.; Wan, W.; Ge, Y.; Yang, R.; Hao, C.; Xiang, J.; Zhang, B.; Zeng, Z. Sulfur-doped black phosphorus field-effect transistors with enhanced stability. *ACS Appl. Mater. Interfaces* **2018**, *10*, 9663–9668. [[CrossRef](#)]
23. Kim, D.-K.; Hong, S.-B.; Jeong, K.; Lee, C.; Kim, H.; Cho, M.-H. p-n junction diode using plasma boron-doped black phosphorus for high-performance photovoltaic devices. *ACS Nano* **2019**, *13*, 1683–1693. [[CrossRef](#)]
24. Liang, Q.; Shi, F.; Xiao, X.; Wu, X.; Huang, K.; Feng, S. In situ growth of CoP nanoparticles anchored on black phosphorus nanosheets for enhanced photocatalytic hydrogen production. *ChemCatChem* **2018**, *10*, 2179–2183. [[CrossRef](#)]
25. Tian, B.; Tian, B.; Smith, B.; Scott, M.; Hua, R.; Lei, Q.; Tian, Y. Supported black phosphorus nanosheets as hydrogen-evolving photocatalyst achieving 5.4% energy conversion efficiency at 353 K. *Nat. Commun.* **2018**, *9*, 1397. [[CrossRef](#)]
26. Bai, L.; Wang, X.; Tang, S.; Kang, Y.; Wang, J.; Yu, Y.; Zhou, Z.K.; Ma, C.; Zhang, X.; Jiang, J. Black phosphorus/platinum heterostructure: A highly efficient photocatalyst for solar-driven chemical reactions. *Adv. Mater.* **2018**, *30*, 1803641. [[CrossRef](#)]
27. Lei, W.; Zhang, T.; Liu, P.; Rodriguez, J.A.; Liu, G.; Liu, M. Bandgap-and local field-dependent photoactivity of Ag/black phosphorus nanohybrids. *ACS Catal.* **2016**, *6*, 8009–8020. [[CrossRef](#)]
28. Yan, J.; Verma, P.; Kuwahara, Y.; Mori, K.; Yamashita, H. Recent progress on black phosphorus-based materials for photocatalytic water splitting. *Small Methods* **2018**, *2*, 1800212. [[CrossRef](#)]
29. Li, Y.; Wu, S.; Zheng, J.; Peng, Y.-K.; Prabhakaran, D.; Taylor, R.A.; Tsang, S.C.E. 2D photocatalysts with tuneable supports for enhanced photocatalytic water splitting. *Mater. Today* **2020**, *41*, 34–43. [[CrossRef](#)]
30. Wang, Y.; Di, Y.; Antonietti, M.; Li, H.; Chen, X.; Wang, X. Excellent visible-light photocatalysis of fluorinated polymeric carbon nitride solids. *Chem. Mater.* **2010**, *22*, 5119–5121. [[CrossRef](#)]
31. Siddiqui, I.; Mittal, H.; Kohli, V.K.; Gautam, P.; Ali, M.; Khanuja, M. Hydrothermally synthesized micron sized, broom-shaped MoSe₂ nanostructures for superior photocatalytic water purification. *Mater. Res. Express* **2018**, *5*, 125020. [[CrossRef](#)]
32. Singhal, C.; Khanuja, M.; Chaudhary, N.; Pundir, C.; Narang, J. Detection of chikungunya virus DNA using two-dimensional MoS₂ nanosheets based disposable biosensor. *Sci. Rep.* **2018**, *8*, 7734. [[CrossRef](#)]
33. Narang, J.; Mishra, A.; Pilloton, R.; Vv, A.; Wadhwa, S.; Pundir, C.S.; Khanuja, M. Development of MoSe₂ nano-urchins as a sensing platform for a selective bio-capturing of Escherichia coli shiga toxin DNA. *Biosensors* **2018**, *8*, 77. [[CrossRef](#)]

34. Chaudhary, N.; Khanuja, M.; Islam, S. Hydrothermal synthesis of MoS₂ nanosheets for multiple wavelength optical sensing applications. *Sens. Actuators A Phys.* **2018**, *277*, 190–198. [[CrossRef](#)]
35. Zhu, M.; Zhai, C.; Fujitsuka, M.; Majima, T. Noble metal-free near-infrared-driven photocatalyst for hydrogen production based on 2D hybrid of black Phosphorus/WS₂. *Appl. Catal. B Environ.* **2018**, *221*, 645–651. [[CrossRef](#)]
36. Ashraf, W.; Fatima, T.; Srivastava, K.; Khanuja, M. Superior photocatalytic activity of tungsten disulfide nanostructures: Role of morphology and defects. *Appl. Nanosci.* **2019**, *9*, 1515–1529. [[CrossRef](#)]
37. Zhang, X.; Pan, R.; Yang, Y.; Han, Q.; Liu, X.; Zhang, C.; Zhou, H.; Han, J.; Gou, J.; Wang, J. High-Performance Photodetector based on a 3D Dirac Semimetal Cd₃As₂/Tungsten Disulfide (WS₂) van der Waals Heterojunction. *Adv. Photonics Res.* **2021**, *2*, 2000194. [[CrossRef](#)]
38. Reddy, D.A.; Kim, E.H.; Gopannagari, M.; Kim, Y.; Kumar, D.P.; Kim, T.K. Few layered black phosphorus/MoS₂ nanohybrid: A promising co-catalyst for solar driven hydrogen evolution. *Appl. Catal. B Environ.* **2019**, *241*, 491–498. [[CrossRef](#)]
39. Yanalak, G.; Eroglu, Z.; Yilmaz, S.; Bas, S.Z.; Metin, O.; Patir, I.H. Metal doped black phosphorus/molybdenum disulfide (BP/MoS₂-Y (Y: Ni, Co)) heterojunctions for the photocatalytic hydrogen evolution and electrochemical nitrite sensing applications. *Int. J. Hydrogen Energy* **2023**, *48*, 14238–14254. [[CrossRef](#)]
40. Boppella, R.; Yang, W.; Tan, J.; Kwon, H.-C.; Park, J.; Moon, J. Black phosphorus supported Ni₂P co-catalyst on graphitic carbon nitride enabling simultaneous boosting charge separation and surface reaction. *Appl. Catal. B Environ.* **2019**, *242*, 422–430. [[CrossRef](#)]
41. Zhang, S.; Chen, S.; Liu, D.; Zhang, J.; Peng, T. Layered WS₂/WO₃ Z-scheme photocatalyst constructed via an in situ sulfurization of hydroxyl WO₃ nanoplates for efficient H₂ generation. *Appl. Surf. Sci.* **2020**, *529*, 147013. [[CrossRef](#)]
42. Liu, W.; Benson, J.; Dawson, C.; Strudwick, A.; Raju, A.P.A.; Han, Y.; Li, M.; Papakonstantinou, P. The effects of exfoliation, organic solvents and anodic activation on the catalytic hydrogen evolution reaction of tungsten disulfide. *Nanoscale* **2017**, *9*, 13515–13526. [[CrossRef](#)]
43. Mahler, B.; Hoepfner, V.; Liao, K.; Ozin, G.A. Colloidal synthesis of 1T-WS₂ and 2H-WS₂ nanosheets: Applications for photocatalytic hydrogen evolution. *J. Am. Chem. Soc.* **2014**, *136*, 14121–14127. [[CrossRef](#)] [[PubMed](#)]
44. Zhou, P.; Xu, Q.; Li, H.; Wang, Y.; Yan, B.; Zhou, Y.; Chen, J.; Zhang, J.; Wang, K. Fabrication of Two-Dimensional Lateral Heterostructures of WS₂/WO₃·H₂O Through Selective Oxidation of Monolayer WS₂. *Angew. Chem.* **2015**, *127*, 15441–15445. [[CrossRef](#)]
45. Eroglu, Z.; Ozer, M.S.; Kubanaliev, T.; Kilic, H.; Metin, Ö. Synergism between few-layer black phosphorus and graphitic carbon nitride enhances the photoredox C–H arylation under visible light irradiation. *Catal. Sci. Technol.* **2022**, *12*, 5379–5389. [[CrossRef](#)]
46. Xu, S.; Li, D.; Wu, P. One-pot, facile, and versatile synthesis of monolayer MoS₂/WS₂ quantum dots as bioimaging probes and efficient electrocatalysts for hydrogen evolution reaction. *Adv. Funct. Mater.* **2015**, *25*, 1127–1136. [[CrossRef](#)]
47. Liu, F.; Shi, R.; Wang, Z.; Weng, Y.; Che, C.M.; Chen, Y. Direct Z-scheme hetero-phase junction of black/red phosphorus for photocatalytic water splitting. *Angew. Chem.* **2019**, *131*, 11917–11921. [[CrossRef](#)]
48. Zheng, Y.; Yu, Z.; Ou, H.; Asiri, A.M.; Chen, Y.; Wang, X. Black phosphorus and polymeric carbon nitride heterostructure for photoinduced molecular oxygen activation. *Adv. Funct. Mater.* **2018**, *28*, 1705407. [[CrossRef](#)]
49. Li, Y.; Ding, L.; Yin, S.; Liang, Z.; Xue, Y.; Wang, X.; Cui, H.; Tian, J. Photocatalytic H₂ evolution on TiO₂ assembled with Ti₃C₂ MXene and metallic 1T-WS₂ as co-catalysts. *Nano-Micro Lett.* **2020**, *12*, 6. [[CrossRef](#)]
50. Sang, Y.; Zhao, Z.; Zhao, M.; Hao, P.; Leng, Y.; Liu, H. From UV to near-infrared, WS₂ nanosheet: A novel photocatalyst for full solar light spectrum photodegradation. *Adv. Mater.* **2015**, *27*, 363–369. [[CrossRef](#)]
51. Wu, S.; Wang, Y. Construction of C@WS₂/g-C₃N₄ Z-scheme photocatalyst with C film as an effective electron mediator and its enhanced degradation of 2, 4-dichlorophenol under visible light. *Chemosphere* **2021**, *273*, 129746. [[CrossRef](#)]
52. Lai, Z.; He, Q.; Tran, T.H.; Repaka, D.; Zhou, D.-D.; Sun, Y.; Xi, S.; Li, Y.; Chaturvedi, A.; Tan, C. Metastable 1T'-phase group VIB transition metal dichalcogenide crystals. *Nat. Mater.* **2021**, *20*, 1113–1120. [[CrossRef](#)]
53. Cha, J.-H.; Choi, S.-J.; Yu, S.; Kim, I.-D. 2D WS₂-edge functionalized multi-channel carbon nanofibers: Effect of WS₂ edge-abundant structure on room temperature NO₂ sensing. *J. Mater. Chem. A* **2017**, *5*, 8725–8732. [[CrossRef](#)]
54. Kotta, A.; Kim, E.-B.; Ameen, S.; Shin, H.-S.; Seo, H.K. Communication—Ultra-small NiO nanoparticles grown by low-temperature process for electrochemical application. *J. Electrochem. Soc.* **2020**, *167*, 167517. [[CrossRef](#)]
55. Cai, L.; Qiu, B.; Lin, Z.; Wang, Y.; Ma, S.; Wang, M.; Tsang, Y.H.; Chai, Y. Active site engineering of Fe- and Ni-sites for highly efficient electrochemical overall water splitting. *J. Mater. Chem. A* **2018**, *6*, 21445–21451. [[CrossRef](#)]
56. Lin, R.; Salehi, M.; Guo, J.; Seifitokaldani, A. High oxidation state enabled by plated Ni-P achieves superior electrocatalytic performance for 5-hydroxymethylfurfural oxidation reaction. *iScience* **2022**, *25*, 104744. [[CrossRef](#)]
57. Liang, H.; Gandhi, A.N.; Xia, C.; Hedhili, M.N.; Anjum, D.H.; Schwingenschlogl, U.; Alshareef, H.N. Amorphous NiFe-OH/NiFeP electrocatalyst fabricated at low temperature for water oxidation applications. *ACS Energy Lett.* **2017**, *2*, 1035–1042. [[CrossRef](#)]
58. Grosvenor, A.P.; Biesinger, M.C.; Smart, R.S.C.; McIntyre, N.S. New interpretations of XPS spectra of nickel metal and oxides. *Surf. Sci.* **2006**, *600*, 1771–1779. [[CrossRef](#)]
59. Xie, J.; Yang, Y.; Li, G.; Xia, H.; Wang, P.; Sun, P.; Li, X.; Cai, H.; Xiong, J. One-step sulfuration synthesis of hierarchical NiCo₂S₄@NiCo₂S₄ nanotube/nanosheet arrays on carbon cloth as advanced electrodes for high-performance flexible solid-state hybrid supercapacitors. *RSC Adv.* **2019**, *9*, 3041–3049. [[CrossRef](#)]
60. Wu, D.; Wei, Y.; Ren, X.; Ji, X.; Liu, Y.; Guo, X.; Liu, Z.; Asiri, A.M.; Wei, Q.; Sun, X. Co(OH)₂ nanoparticle-encapsulating conductive nanowires array: Room-temperature electrochemical preparation for high-performance water oxidation electrocatalysis. *Adv. Mater.* **2018**, *30*, 1705366. [[CrossRef](#)]

61. Li, X.-C.; She, F.-S.; Shen, D.; Liu, C.-P.; Chen, L.-H.; Li, Y.; Deng, Z.; Chen, Z.-H.; Wang, H.-E. Coherent nanoscale cobalt/cobalt oxide heterostructures embedded in porous carbon for the oxygen reduction reaction. *RSC Adv.* **2018**, *8*, 28625–28631. [[CrossRef](#)]
62. Liang, Z.; Xue, Y.; Wang, X.; Zhou, Y.; Zhang, X.; Cui, H.; Cheng, G.; Tian, J. Co doped MoS₂ as cocatalyst considerably improved photocatalytic hydrogen evolution of g-C₃N₄ in an alkaline environment. *Chem. Eng. J.* **2021**, *421*, 130016. [[CrossRef](#)]
63. Fang, H.-B.; Zhang, X.-H.; Wu, J.; Li, N.; Zheng, Y.-Z.; Tao, X. Fragmented phosphorus-doped graphitic carbon nitride nanoflakes with broad sub-bandgap absorption for highly efficient visible-light photocatalytic hydrogen evolution. *Appl. Catal. B Environ.* **2018**, *225*, 397–405. [[CrossRef](#)]
64. Wang, H.; Zhang, J.; Jin, X.; Wang, X.; Zhang, F.; Xue, J.; Li, Y.; Li, J.; Zhang, G. General surface grafting strategy-derived carbon-modified graphitic carbon nitride with largely enhanced visible light photocatalytic H₂ evolution coupled with benzyl alcohol oxidation. *J. Mater. Chem. A* **2021**, *9*, 7143–7149. [[CrossRef](#)]
65. Wang, Z.; Fan, J.; Cheng, B.; Yu, J.; Xu, J. Nickel-based cocatalysts for photocatalysis: Hydrogen evolution, overall water splitting and CO₂ reduction. *Mater. Today Phys.* **2020**, *15*, 100279. [[CrossRef](#)]
66. Gonce, M.K.; Dogru, M.; Aslan, E.; Ozel, F.; Patir, I.H.; Kus, M.; Ersoz, M. Photocatalytic hydrogen evolution based on Cu₂ZnSnS₄, Cu₂ZnSnSe₄ and Cu₂ZnSnSe₄–xSx nanofibers. *RSC Adv.* **2015**, *5*, 94025–94028. [[CrossRef](#)]
67. Abe, R.; Hara, K.; Sayama, K.; Domen, K.; Arakawa, H. Steady hydrogen evolution from water on Eosin Y-fixed TiO₂ photocatalyst using a silane-coupling reagent under visible light irradiation. *J. Photochem. Photobiol. A Chem.* **2000**, *137*, 63–69. [[CrossRef](#)]
68. Kimura, K.; Miwa, T.; Imamura, M. The radiolysis and photolysis of methanolic solutions of eosin. I. The γ -radiolysis of neutral and alkaline solutions. *Bull. Chem. Soc. Jpn.* **1970**, *43*, 1329–1336. [[CrossRef](#)]
69. Eken Korkut, S.; Kucukkececi, H.; Metin, O. Mesoporous graphitic carbon nitride/black phosphorus/AgPd alloy nanoparticles ternary nanocomposite: A highly efficient catalyst for the methanolysis of ammonia borane. *ACS Appl. Mater. Interfaces* **2020**, *12*, 8130–8139. [[CrossRef](#)]
70. Hari, D.P.; König, B. Synthetic applications of eosin Y in photoredox catalysis. *Chem. Commun.* **2014**, *50*, 6688–6699. [[CrossRef](#)]
71. Srivastava, V.; Singh, P.P. Eosin Y catalysed photoredox synthesis: A review. *RSC Adv.* **2017**, *7*, 31377–31392. [[CrossRef](#)]
72. Acar, E.G.; Yilmaz, S.; Eroglu, Z.; Aslan, E.; Metin, Ö.; Patir, İ.H. Solar-light-driven Photocatalytic Hydrogen Evolution Activity of gCN/WS₂ Heterojunctions Incorporated with the First-row Transition Metals. *J. Alloys Compd.* **2023**, *950*, 169753. [[CrossRef](#)]
73. Yilmaz, S.; Acar, E.G.; Yanalak, G.; Aslan, E.; Kılıç, M.; Patir, İ.H.; Metin, Ö. Enhanced hydrogen evolution by using ternary nanocomposites of mesoporous carbon nitride/black phosphorus/transition metal nanoparticles (m-gCN/BP-M; M = Co, Ni, and Cu) as photocatalysts under visible light: A comparative experimental and theoretical study. *Appl. Surf. Sci.* **2022**, *593*, 153398.
74. Xu, Q.; Zhang, L.; Cheng, B.; Fan, J.; Yu, J. S-scheme heterojunction photocatalyst. *Chem* **2020**, *6*, 1543–1559. [[CrossRef](#)]
75. Choi, S.K.; Kim, S.; Ryu, J.; Lim, S.K.; Park, H. Titania nanofibers as a photo-antenna for dye-sensitized solar hydrogen. *Photochem. Photobiol. Sci.* **2012**, *11*, 1437–1444. [[CrossRef](#)]
76. Peimyoo, N.; Shang, J.; Cong, C.; Shen, X.; Wu, X.; Yeow, E.K.; Yu, T. Nonblinking, intense two-dimensional light emitter: Monolayer WS₂ triangles. *ACS Nano* **2013**, *7*, 10985–10994. [[CrossRef](#)]
77. Reddy, D.A.; Park, H.; Ma, R.; Kumar, D.P.; Lim, M.; Kim, T.K. Heterostructured WS₂-MoS₂ Ultrathin Nanosheets Integrated on CdS Nanorods to Promote Charge Separation and Migration and Improve Solar-Driven Photocatalytic Hydrogen Evolution. *ChemSusChem* **2017**, *10*, 1563–1570. [[CrossRef](#)] [[PubMed](#)]
78. Yüzer, A.C.; Genc, E.; Kurtay, G.; Yanalak, G.; Aslan, E.; Harputlu, E.; Ocakoglu, K.; Patir, I.H.; Ince, M. Imidazole substituted Zinc (ii) phthalocyanines for co-catalyst-free photoelectrochemical and photocatalytic hydrogen evolution: Influence of the anchoring group. *Chem. Commun.* **2021**, *57*, 9196–9199. [[CrossRef](#)] [[PubMed](#)]
79. Stan, M.C.; von Zamory, J.; Passerini, S.; Nilges, T.; Winter, M. Puzzling out the origin of the electrochemical activity of black P as a negative electrode material for lithium-ion batteries. *J. Mater. Chem. A* **2013**, *1*, 5293–5300. [[CrossRef](#)]
80. Zhao, G.; Wang, T.; Shao, Y.; Wu, Y.; Huang, B.; Hao, X. A Novel Mild Phase-Transition to Prepare Black Phosphorus Nanosheets with Excellent Energy Applications. *Small* **2017**, *13*, 1602243. [[CrossRef](#)] [[PubMed](#)]
81. Ran, J.; Zhu, B.; Qiao, S.-Z. Phosphorene Co-catalyst Advancing Highly Efficient Visible-Light Photocatalytic Hydrogen Production. *Angew. Chem. Int. Ed.* **2017**, *56*, 10373–10377. [[CrossRef](#)]
82. Zhu, M.; Sun, Z.; Fujitsuka, M.; Majima, T. Z-Scheme Photocatalytic Water Splitting on a 2D Heterostructure of Black Phosphorus/Bismuth Vanadate Using Visible Light. *Angew. Chem. Int. Ed.* **2018**, *57*, 2160–2164. [[CrossRef](#)] [[PubMed](#)]
83. Zhu, M.; Fujitsuka, M.; Zeng, L.; Liu, M.; Majima, T. Dual function of graphene oxide for assisted exfoliation of black phosphorus and electron shuttle in promoting visible and near-infrared photocatalytic H₂ evolution. *Appl. Catal. B* **2019**, *256*, 117864. [[CrossRef](#)]
84. Huang, Y.; Lu, H.; Wang, B.; He, W.; Dong, H.; Sui, L.; Gan, Z.; Ma, S.; Pang, B.; Dong, L.; et al. Synthesis and photocatalytic performance of MoS₂/Polycrystalline black phosphorus heterojunction composite. *Int. J. Hydrogen Energy* **2021**, *46*, 3530–3538. [[CrossRef](#)]
85. Shi, L.; Wang, Y.; Yan, Y.; Liu, F.; Huang, Z.; Ren, X.; Zhang, H.; Li, Y.; Ye, J. Synergy of heterojunction and interfacial strain for boosting photocatalytic H₂ evolution of black phosphorus nanosheets. *J. Colloid Interface Sci.* **2022**, *627*, 969–977. [[CrossRef](#)] [[PubMed](#)]

Disclaimer/Publisher's Note: The statements, opinions and data contained in all publications are solely those of the individual author(s) and contributor(s) and not of MDPI and/or the editor(s). MDPI and/or the editor(s) disclaim responsibility for any injury to people or property resulting from any ideas, methods, instructions or products referred to in the content.